EES Catalysis

PAPER

View Article Online
View Journal

Check for updates

Cite this: DOI: 10.1039/d5ey00359h

Structure–function evolution of transition metal molybdate catalysts driven by hydrodeoxygenation environment

Gabriel B. Báfero, †[a] Guilherme B. Strapasson, [ab] Leonardo S. Sousa,‡[a] James S. Hayward,[c] Pedro B. M. Nunes,[a] Davi S. Leite,[a] David J. Morgan, [cd] Jonathan K. Bartley *[c] and Daniela Zanchet *[a]

Received 19th December 2025,
Accepted 26th February 2026

DOI: 10.1039/d5ey00359h

rsc.li/eescatalysis

Bulk mixed metal oxides are increasingly explored as sustainable catalysts, yet their behaviour under hydrodeoxygenation (HDO) environments remains poorly understood. Here, we reveal how first-row transition metal molybdates (MMo, M = Mn, Fe, Co, Cu, Zn) undergo metal-dependent restructuring under acetone HDO, leading to the emergence of functional Mo-rich phases with distinct redox and catalytic properties. Catalytic testing combined with comprehensive post-reaction characterization shows that HDO conditions promote the formation of substoichiometric molybdenum species (MoO_xC_y) whose abundance and distribution are governed by the reducibility of the incorporated metal. These dynamically generated phases promote efficient deoxygenation through multiple pathways and explain the broad reactivity trends across the MMo series. Our findings demonstrate that hydrodeoxygenation can direct the self-assembly of transition metal molybdates into catalytically versatile architectures, providing generalizable principles for designing redox-active oxide catalysts for biomass valorization and other oxygen-rich feedstocks.

Open Access Article. Published on 27 April 2026. Downloaded on 5/21/2026 11:31:09 AM.
This article is licensed under a Creative Commons Attribution-NonCommercial 3.0 Unported Licence.

Broader context

The transition to a low-carbon chemical sector requires efficient strategies to convert biomass-derived oxygenates into energy carriers and value-added chemicals. Hydrodeoxygenation (HDO) is central to this transformation, yet the development of robust, earth-abundant catalysts capable of operating under the reducing, carbon-rich conditions imposed by real bio-oil streams remains a major challenge. Transition metal molybdates are appealing candidates due to their redox properties and compositional tunability, but their behaviour under HDO environments, and how this affects catalytic function, has been poorly understood. This study reveals that first-row metal molybdates undergo metal-dependent restructuring into functional Mo-rich phases that efficiently remove oxygen through distinct pathways. By uncovering how reaction environments can direct the emergence of catalytically relevant architectures, our findings provide new design principles for redox-active oxide catalysts and advance the development of sustainable processes for biomass valorization and renewable fuel production.

1. Introduction

The hydrodeoxygenation (HDO) of biomass-derived compounds is a benchmark reaction in the conversion of renewable feedstocks into fuels and platform chemicals. Although biomass is abundant and chemically diverse,[1] its high oxygen content poses significant challenges for efficient upgrading.[2] The liquid fraction obtained from fast pyrolysis, commonly referred to as bio-oil, contains a complex mixture of oxygenated species including ketones, aldehydes, carboxylic acids, furans, sugars, and phenolic aromatics.[3] The structural diversity of these compounds demands multifunctional catalysts capable of performing selective C–O bond cleavage while suppressing overhydrogenation and undesired side reactions.[4–6]

[a] Institute of Chemistry, University of Campinas (UNICAMP), Campinas, 13083-970, Brazil. E-mail: zanchet@unicamp.br
[b] Brazilian Synchrotron Light Laboratory (LNLS), Brazilian Center for Research in Energy and Materials (CNPEM), Campinas, 13083-100, Brazil
[c] Cardiff Catalysis Institute (CCI), School of Chemistry, Cardiff University, Cardiff, CF10 3AT, UK. E-mail: bartleyjk@cardiff.ac.uk
[d] HarwellXPS, Research Complex at Harwell (RCaH), Didcot, OX11 OFA, UK
† Present addresses: Brazilian Synchrotron Light Laboratory (LNLS), Brazilian Center for Research in Energy and Materials (CNPEM), Campinas, 13083-100, Brazil.
‡ Present addresses: Research Complex at Harwell (RCaH), Rutherford Appleton Laboratory, Harwell Science and Innovation Campus, Didcot, OX11 0FA, UK.

Open Access Article. Published on 27 April 2026. Downloaded on 5/21/2026 11:31:09 AM.
This article is licensed under a Creative Commons Attribution-NonCommercial 3.0 Unported Licence.

Reducible metal oxides, particularly those based on molybdenum, have garnered increasing attention as potential HDO catalysts.[7–9] Their ability to promote deoxygenation through the reverse Mars–van Krevelen (MvK) mechanism, by generating and restoring oxygen vacancies, enables them to activate and transform oxygenated intermediates efficiently.[10,11] The flexibility of molybdenum oxides redox properties allows fine-tuning of active site properties and catalytic selectivity across a range of reactions.[12–18] Under reducing and carburizing HDO conditions, MoO_3 may evolve into different phases such as MoO_2, MoO_xC_y, and Mo_2C.[9,19,20] These phases, especially the substoichiometric ones, can introduce varied functionalities, including acidic, metallic, and bifunctional sites, which are often essential for complex transformations involved in biomass valorization.[1,21]

Recent studies have expanded the application of molybdenum-based catalysts beyond classical monometallic systems, exploring bimetallic and mixed oxide configurations incorporating first-row transition metals.[22–24] Cu–Mo/C catalysts, for instance, have demonstrated high activity and selectivity in the hydrogenation of methyl oleate to diesel-range hydrocarbons, where the synergy between Cu and Mo was associated with enhanced hydrogenation functionality and dispersion of active sites.[25] Transition metal-doped MoO_3 surfaces, particularly with Fe, Co, Ni, Cu, and Zn, showed different electronic structure and surface reactivity compared with MoO_3 due to substitution of surface Mo atoms by the transition metal dopant, which have facilitated C–O bond activation under reductive environments.[26] In the context of HDO, sulfided Mo-based catalysts promoted with Ni, Fe, Zn, and Cu displayed diverse selectivity patterns for phenolic substrates, reflecting the modifying role of the metal promoter on the deoxygenation pathway.[27] Despite these advances, the structural and mechanistic roles of metal–molybdenum interactions in bulk molybdate systems remain comparatively underexplored.

Although promising, most investigations on molybdenum-based catalysts have concentrated on pure oxides or supported systems, while bulk mixed metal molybdates (MMo) have received far less attention in the context of HDO.[28–31] These materials, well known for their roles in selective oxidation catalysis,[32,33] offer a rich structural framework that could stabilize diverse active sites and promote unique phase transformations under reaction conditions. Moreover, some studies suggest that under reducing environments, MMo systems can undergo restructuring into new phases, including carbides or metal/oxide composites, potentially unlocking novel catalytic behavior.[29,34]

In this context, the present work investigates the catalytic behavior and structural evolution of first-row transition metal molybdates (MMo, where M = Mn, Fe, Co, Cu, Zn) under HDO conditions. Acetone was employed as a model compound due to its prominence in bio-oil matrices and its mechanistic richness, encompassing parallel pathways such as hydrogenation, aldol condensation, dehydration, and direct deoxygenation.[9,35–42] This complexity enables acetone to act not only as a relevant substrate, but also as a mechanistic probe for disentangling the roles of acid sites (AS), hydrogenation/hydrogenolysis sites (HS), and oxygen vacancies (OVS). As illustrated in Scheme 1, the diversity of products formed during acetone HDO allows for a direct evaluation of site-specific functionalities, supporting a comprehensive structure-function analysis of the MMo catalyst series.

By integrating catalytic testing with extensive *ex situ* and *operando* characterization, we uncover how each MMo catalyst undergoes a distinct restructuring pathway under reaction conditions. These findings reveal that the HDO environment itself drives self-directed restructuring of molybdate lattices, leading to the emergence of catalytically versatile architectures whose activity and selectivity emerge from dynamic redox and structural adaptability. Such insights provide a unified framework linking composition, reducibility, and surface evolution to function.

2. Experimental section

2.1. Materials

All the employed reagents were purchased in high purity. Molybdenum(VI) oxide (MoO_3, nanopowder), copper(II) and copper(I) oxides (CuO, nanopowder/Cu_2O, 97%), manganese(II) nitrate tetrahydrate ($Mn(NO_3)_2{\cdot}4H_2O$, $\geq$97.0%), cobalt(II) nitrate hexahydrate ($Co(NO_3)_2{\cdot}6H_2O$, 98%), cooper(II) nitrate (hemi)-pentahydrate ($Cu(NO_3)_2{\cdot}2.5H_2O$, 98%), zinc(II) nitrate hexahydrate ($Zn(NO_3)_2{\cdot}6H_2O$, 98%), and acetone (HPLC Plus Grade, $\geq$99.9%) were obtained from Sigma-Aldrich. Ammonium heptamolybdate tetrahydrate ($(NH_4)_6MoO_7{\cdot}4H_2O$) and iron(III) nitrate nonahydrate ($Fe(NO_3)_3{\cdot}9H_2O$, $\geq$99.0%) were supplied by Supelco.

2.2. Synthesis methods

The first-row transition metal molybdate catalysts (Mn, Fe, Co, Cu, and Zn) were prepared following a standard synthesis described elsewhere.[28] The general procedure involved the dissolution of 2.0 mmol of ammonium heptamolybdate tetrahydrate ($(NH_4)_6MoO_7{\cdot}4H_2O$) in 200 mL of water at 40 °C. Separately, the appropriate amount of each transition metal nitrate (2.0 mmol for Mn, Co, Cu, and Zn, and 1.3 mmol for Fe) was dissolved in 100 mL of water at room temperature. The transition metal solution was added to the molybdate solution dropwise using an autotritrator (5 mL min^{-1}). After the addition, the precipitated mixture was aged for 2 h under vigorous stirring at room temperature, washed with water, dried at 120 °C overnight, and calcined under air (5 °C min^{-1} until 500 °C, 4 h). The catalysts were called MMo, where M corresponds to the first-row transition metal (Mn, Fe, Co, Cu, or Zn).

For further comparison and catalytic testing, a physical mixture of CuO and MoO_3 in a 3Cu : 2Mo molar ratio was prepared by manually grinding the corresponding commercial oxides using a pestle and mortar. Additionally, a CuO/MoO_3 catalyst containing 10 wt% Cu was synthesized *via* wet impregnation. In this procedure, a concentrated aqueous solution of copper nitrate was gradually added dropwise to MoO_3 powder under continuous mixing, until the desired copper loading was

© 2026 The Author(s). Published by the Royal Society of Chemistry

Open Access Article. Published on 27 April 2026. Downloaded on 5/21/2026 11:31:09 AM.
This article is licensed under a Creative Commons Attribution-NonCommercial 3.0 Unported Licence.

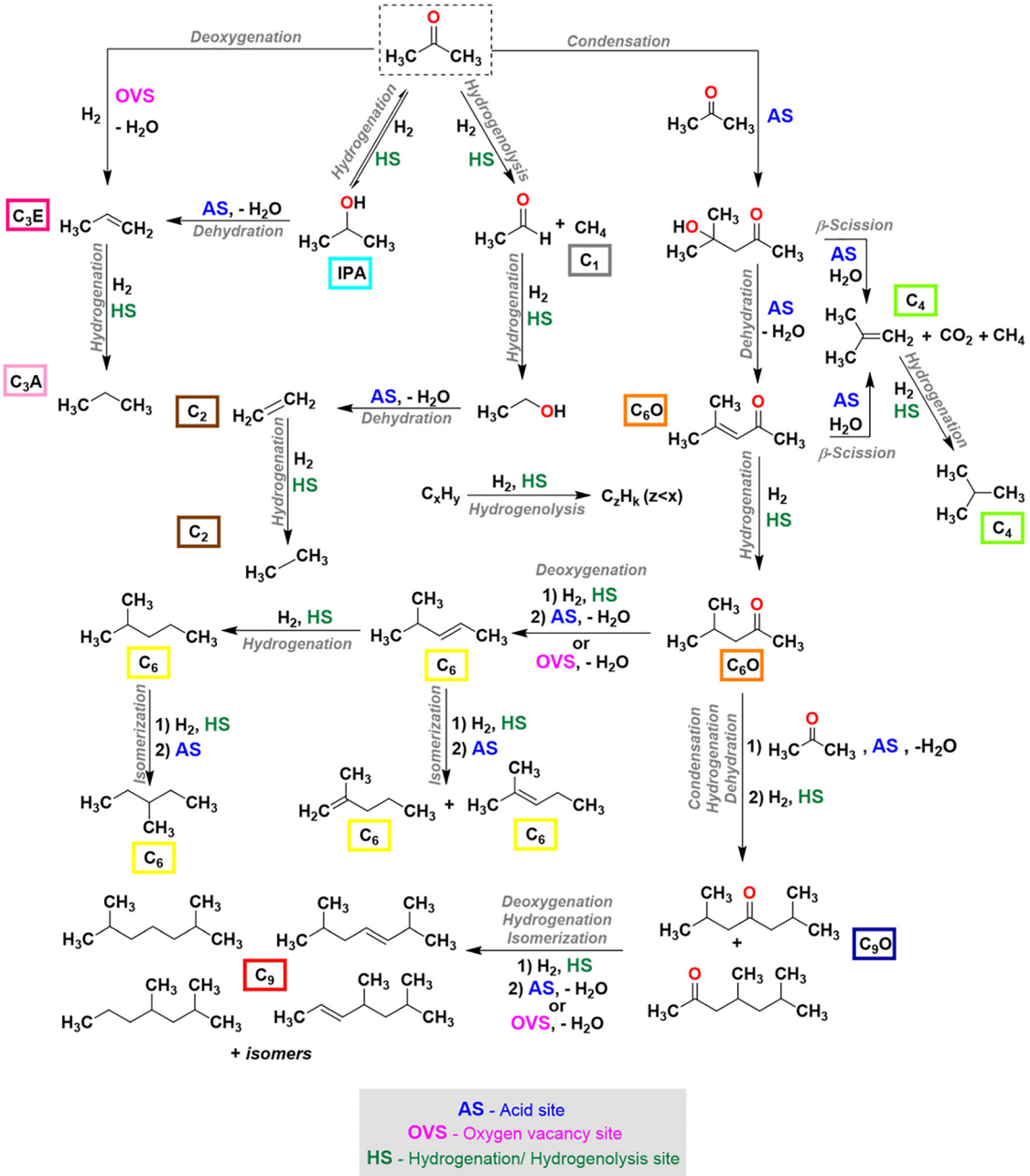

Scheme 1 Adapted reaction network for acetone HDO over MMo catalysts.[9]

fully deposited. The resulting material was dried at 120 °C overnight and then calcined under air atmosphere (5 °C min^{-1} until 500 °C, 4 h).

2.3. Characterization methods

The catalysts were characterized using a combination of bulk, surface, and *operando* techniques, including X-ray diffraction (XRD) and total scattering/PDF analysis, X-ray fluorescence (XRF), X-ray photoelectron spectroscopy (XPS), N_2 physisorption, temperature-programmed reduction (TPR), scanning and transmission electron microscopy (SEM/TEM), and *operando* diffuse reflectance infrared Fourier transform spectroscopy (DRIFTS). These complementary methods were employed to probe phase evolution, surface composition and oxidation states, textural properties, morphology, and dynamic surface chemistry under reaction conditions. Full experimental details and instrumental parameters are provided in the SI.

2.4. Catalytic evaluation

The gas-phase acetone HDO reaction was conducted in a plug-flow tubular reactor fitted with a quartz tube (inner diameter: 8.1 mm). The catalytic bed consisted of 50 mg of catalyst mixed with 150 mg of quartz powder (<100 mesh) as diluent. Acetone was introduced *via* a saturation flask (2.4 mL min^{-1} of acetone)

Open Access Article. Published on 27 April 2026. Downloaded on 5/21/2026 11:31:09 AM. This article is licensed under a Creative Commons Attribution-NonCommercial 3.0 Unported Licence.

using He as the carrier gas. Hydrogen was co-fed at 51 mL min^{-1} (corresponding to a 21 : 1 molar H_2 : acetone ratio), with He added to balance the total flow to 100 mL min^{-1}. The weight hourly space velocity (WHSV) was equal to 7.32 $g_{acetone}\ g_{catalyst}^{-1}\ h^{-1}$ under these conditions. Two main catalytic tests were performed: (i) isothermal tests to evaluate the effect of time on stream (TOS) over 6 h, and (ii) temperature-dependent experiments with 1 h plateaus to assess catalytic activity as a function of temperature. Prior to acetone introduction, the sample was heated under H_2 to the target temperature at a rate of 10 °C min^{-1}. For selected post-reaction characterizations (XRD, HRTEM, PDF, and *operando* DRIFTS), the CuMo catalyst was subjected to the same reaction conditions without diluent, using approximately 400 mg of material; temperature-dependent tests were conducted with 1 h plateaus at each temperature step (175, 200, and 300 °C). A fresh catalyst charge was used in each experiment. An additional catalytic test was performed by treating commercial MoO_3 at 400 °C for 30 min under acetone HDO conditions, then cooling it down to 200 °C under He and conducting temperature-dependent experiments as previously described.

The reaction products were analyzed by an online gas chromatograph (GC; Agilent Technologies, model 7890A) equipped with two columns, HP-1 and HP-MOLESIEVE, with FID and TCD detectors. Acetone conversion, mass-normalized acetone consumption rate, products' distribution, and carbon balances were calculated using eqn (1)–(4). The mass-normalized rate was included to facilitate a rate-based comparison of catalytic activity under identical feed and space velocity, complementing conversion values and acknowledging the evolving nature of the catalytically active surface.

$$\text{Acetone conversion (C} - \text{mol\%)} = \frac{\text{carbon moles of consumed reactant}}{\text{carbon moles in reactant feed}} \times 100\% \quad (1)$$

$$\text{Acetone consumption rate} \left(\text{mmol}_{\text{acetone}}\ g_{\text{catalyst}}^{-1}\ h^{-1}\right) = \frac{\text{WHSV} \cdot \text{acetone conversion}}{\text{acetone molar mass}} \quad (2)$$

$$\text{Product distribution (C} - \text{mol\%)} = \frac{\text{carbon moles of product}}{\text{carbon moles of all products}} \times 100\% \quad (3)$$

$$\text{Carbon balance} = \frac{\text{carbon moles of all products}}{\text{carbon moles in reactant feed}} \quad (4)$$

The main products detected during acetone HDO were methane (C_1), ethene/ethane (C_2), propane (C_3A), propene (C_3E), isobutene/isobutane and isomers (C_4), hexene/hexane and isomers (C_6), nonene/nonane and isomers (C_9), carbon dioxide (CO_2), isopropyl alcohol (IPA), acetaldehyde (C_2H_4O), methyl isobutyl ketone and isomers (C_6O), and diisobutyl ketone and isomers (C_9O), see Scheme 1. To simplify the analysis and discussion, the following groupings will be used: direct deoxygenation products (C_3E) as DDP; coupling deoxygenated products (C_4, C_6, C_9) as CDP; hydrogenation/hydrogenolysis products (C_1, C_2, C_3A, IPA) as HHP; and oxygenated products (CO_2, C_2HO, C_6O, C_9O) as OP, see Scheme 2. The full catalytic data is provided in the SI. Carbon balances presented slight decreases over time on stream (TOS) and/or at higher temperatures, but remained above 85%.

3. Results and discussion

3.1. Synthesis and structural characterization of MMo catalysts

First-row transition metal molybdates (MMo, where M = Mn^{2+}, Fe^{3+}, Co^{2+}, Cu^{2+}, Zn^{2+}) represent a structurally diverse class of mixed oxides, typically composed of Mo^{6+} species in octahedral coordination and M^{2+}/M^{3+} cations occupying various local geometries depending on composition and lattice symmetry.[43,44] Unlike classical perovskite or spinel-type oxides, which exhibit highly ordered A- and B-site frameworks,[32] molybdates often adopt more flexible architectures shaped by the size and charge of the metal center.[32]

Powder XRD patterns displayed in Fig. 1 confirmed the formation of well-defined crystalline phases. MnMo, FeMo, and CoMo matched known monoclinic molybdate structures (ICSD 15615, 16402, and 118340, respectively), ZnMo exhibited

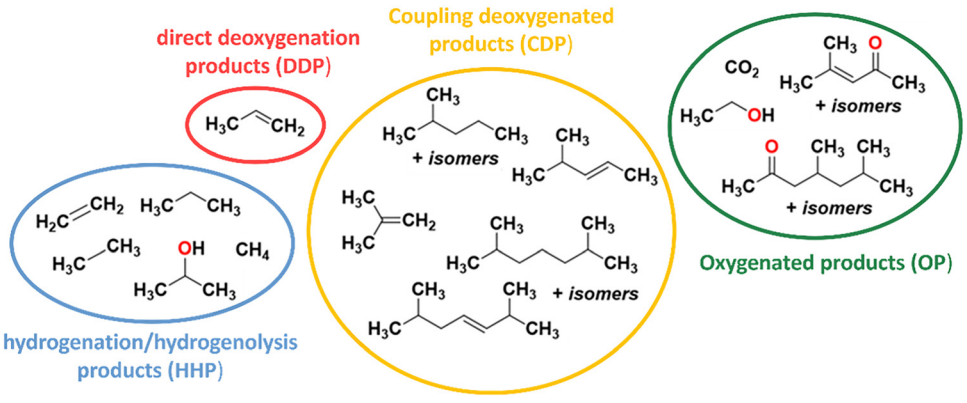

Scheme 2 Representation of acetone HDO main products separated into four groups.

© 2026 The Author(s). Published by the Royal Society of Chemistry

Open Access Article. Published on 27 April 2026. Downloaded on 5/21/2026 11:31:09 AM.
This article is licensed under a Creative Commons Attribution-NonCommercial 3.0 Unported Licence.

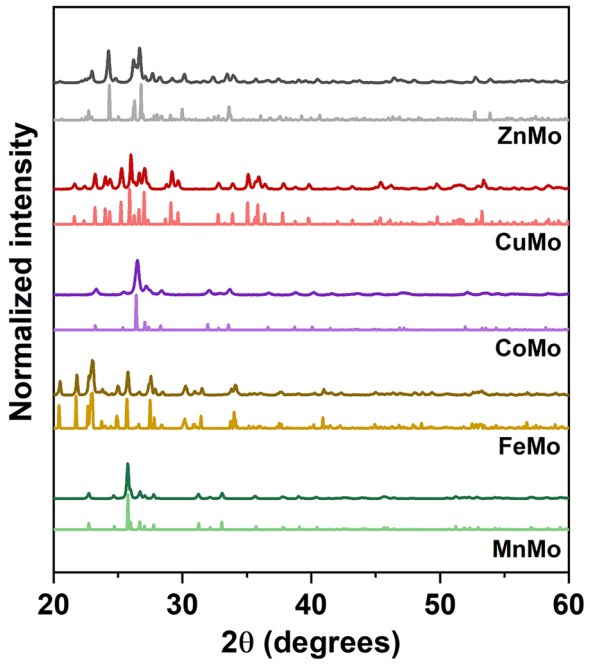

Fig. 1 Powder XRD patterns (dark colored) of the first-row transition metal molybdate catalysts (MMo): MnMo, FeMo, CoMo, CuMo, and ZnMo. Correspondent simulated patterns (light colored) obtained from the ICSD database are shown for reference.[45]

a triclinic pattern (ICSD 17030), and CuMo crystallized as $Cu_3Mo_2O_9$ with an orthorhombic unit cell (ICSD 2836), indicating a structural deviation from the more common $MMoO_4$-type phase.

BET surface areas (in the range of 4–22 $m^2\ g^{-1}$, Table S1) were consistent with the dense, non-porous nature of bulk mixed oxides.[32] SEM analysis (Fig. S1) revealed distinct morphological trends. MnMo formed elongated rods ($\sim$2 μm),[28,46] while FeMo, CoMo, and CuMo appeared as irregular aggregates of smaller crystallites.[47–50] ZnMo crystallized as compact, intergrown platelets typically smaller than 1 μm.[28]

Table 1 compiles the key crystallographic parameters of the obtained phases, derived from ICSD references. All materials feature Mo^{6+} in distorted octahedral or tetrahedral environments. Mo–Mo distances within the unite cell span from 3.45 to 5.00 Å, reflecting different connectivity patterns between molybdenum centers. Mo–M distances also vary substantially, 3.2–5.0 Å, depending on the cation radius and local symmetry. Mo–O bond lengths for shortest interactions range from 1.65 to 2.00 Å, consistent with Mo^{6+}–O bonding, while M–O distances (1.73–2.00 Å) reflect the coordination variability among M cations.

These structural parameters hint at deeper differences in the chemical behavior and redox dynamics of each material. For example, CuMo's comparatively short M–M and M–O distances and highly distorted lattice (with a small unit cell and 12 Cu^{2+} ions per $Cu_3Mo_2O_9$ unit) may facilitate structural collapse and phase segregation under reactive conditions. In contrast, MnMo's more rigid monoclinic lattice and longer interatomic distances could point out to a greater structural stability. The intrinsic reducibility of the constituent metals further modulates this behavior: copper exhibits the highest reducibility, readily forming metallic Cu^0 under mild conditions, whereas manganese is considerably more resistant to reduction, stabilizing its oxide framework even at elevated temperatures.

Altogether, data findings highlight the structural variability intrinsic to first-row transition metal molybdates. Differences in local geometry, bonding distances, and unit cell metrics set the foundation for understanding their thermal and chemical behavior, which will be further explored.

3.2. Catalytic activity and phase evolution of MMo catalysts under acetone HDO

3.2.1. Temperature-dependent and isothermal HDO performance of MMo catalysts. The acetone HDO reaction over MMo catalysts produced a diverse set of products, including C_1, C_2, C_3A, C_3E, C_4, C_6, C_6O, C_9, C_9O, and IPA that can be grouped into distinct mechanistic families, as summarized in Scheme 2. According to the proposed reaction pathways (Scheme 1), C_6O and C_9O are acetone condensation-derived oxygenated products (OP) formed primarily *via* acid-catalyzed aldol condensation, followed by dehydration (acid site, AS) and hydrogenation (hydrogenation site, HS) steps. C_3E belongs to the acetone direct deoxygenation products (DDP), which can arise either from reactions involving oxygen vacancies (OVS), which are undercoordinated sites, or from hydrogenation–dehydration pathways requiring both HS and AS. Acetone hydrogenolysis/hydrogenation products (HHP), including C_1, C_2, C_3A, and IPA, are mainly formed *via* C–C or C–O bond scission on metal-like HS. Finally, acetone coupling-derived products (CDP) such as C_6 and C_9 result from further deoxygenation of C_6O and C_9O, while β-scission of C_6O may generate C_4. This classification allows product distributions to be mechanistically linked to the diversity and accessibility of catalytic sites across the MMo series.

Under isothermal operation at 400 °C, distinct catalytic behaviors were observed (Fig. 2, Table 2, and detailed data in Tables S2–S7). MoO_3, included as a benchmark, showed moderate acetone conversion (39% decreasing to 22% after 6 h), corresponding to relatively low acetone consumption rate (decreasing from 49 to 28 $mmol_{acetone}\ g_{cat}^{-1}\ h^{-1}$),with product distribution dominated by DDP and a small fraction of CDP. This modest rate highlights that, despite measurable conversion, MoO_3 remains kinetically limited under these conditions, consistent with its known restructuring at reaction temperatures into a mixture of crystalline MoO_2 and amorphous MoO_xC_y domains,[9] which display both redox and acid functionalities but require thermal activation under reactional atmosphere to reach catalytic relevance.

MnMo was the least active among the MMo series, achieving 8% conversion at 400 °C, corresponding to values below 11 $mmol_{acetone}\ g_{cat}^{-1}\ h^{-1}$, and showing > 90% selectivity to OP. This low mass-normalized rate confirms that manganese incorporation suppresses not only conversion but also the intrinsic rate of acetone transformation. In contrast, FeMo

Open Access Article. Published on 27 April 2026. Downloaded on 5/21/2026 11:31:09 AM.
This article is licensed under a Creative Commons Attribution-NonCommercial 3.0 Unported Licence.

Table 1 Relevant structural properties of the obtained molybdate structures

	MoO_3	$MnMoO_4$	$Fe_2(MoO_4)_3$	$CoMoO_4$	$ZnMoO_4$	$Cu_3Mo_2O_9$
collCode	166363	15615	16402	118340	17030	2836
Geometry	Orthorombic	Monoclinic	Monoclinic	Monoclinic	Triclinic	Orthorombic
Space Group	*Pbnm*	*C*12/*m*1	*P*1211	*C*12/*m*1	$P\bar{1}$	*Pnam*
Mo site	Mo^{6+} at O_h	Mo^{6+} at T_d	Mo^{6+} at T_d	Mo^{6+} at T_d	Mo^{6+} at T_d	Mo^{6+} at T_d
Mo–Mo distance	[a]3.45 Å	[a]3.97 Å	[a]4.25 Å	[a]4.09 Å	[a]3.85 Å	[a]4.15 Å
	[b]4.95 Å	[b]5.00 Å	[b]4.98 Å	[b]4.89 Å	[b]4.93 Å	[b]4.78 Å
	[c]4.95 Å	[c]4.87 Å	[c]4.63 Å	[c]4.75 Å	[c]4.40 Å	[c]4.65 Å
Mo–M distance	—	[a]3.55 Å	[a]3.44 Å	[a]3.46 Å	[a]3.42 Å	[a]3.54 Å
		[b]4.80 Å	[b]4.94 Å	[b]4.63 Å	[b]4.96 Å	[b]4.81 Å
		[c]3.55 Å	[c]3.61 Å	[c]3.45 Å	[c]3.45 Å	[c]3.45 Å
M–M distance	—	[a]3.25 Å	[a]5.09 Å	[a]3.16 Å	[a]3.10 Å	[a]2.86 Å
		[b]3.55 Å	[b]6.75 Å	[b]3.32 Å	[b]4.99 Å	[b]4.99 Å
		[c]3.25 Å	[c]6.35 Å	[c]3.16 Å	[c]3.15 Å	[c]2.85 Å
Mo–O distance	[a]1.65 Å	[a]1.58 Å	[a]1.61 Å	[a]1.72 Å	[a]1.71 Å	[a]1.70 Å
	[b]4.95 Å	[b]4.97 Å	[b]4.90 Å	[b]4.98 Å	[b]4.95 Å	[b]5.00 Å
	[c]4.05 Å	[c]4.28 Å	[c]4.38 Å	[c]4.05 Å	[c]4.35 Å	[c]4.35Å
M–O distance	—	[a]2.00 Å	[a]1.91 Å	[a]1.98 Å	[a]1.95 Å	[a]1.73 Å
		[b]4.98 Å	[b]4.99 Å	[b]4.93 Å	[b]4.99 Å	[b]4.92 Å
		[c]4.60 Å	[c]4.90 Å	[c]4.65 Å	[c]4.65 Å	[c]4.35 Å
Lattice parameter	a = 3.96 Å	a = 10.47 Å	a = 15.69Å	a = 10.25Å	a = 9.63Å	a = 7.66Å
	b = 13.86 Å	b = 9.52 Å	b = 9.24Å	b = 9.30Å	b = 6.97Å	b = 14.61Å
	c = 3.70 Å	c = 7.14 Å	c = 18.22Å	c = 7.04Å	c = 8.37Å	c = 6.88Å
No. of atoms/cell	4 Mo^{6+}	4 Mo^{6+}	12 Mo^{6+}	4 Mo^{6+}	4 Mo^{6+}	8 Mo^{6+}
	12 O^{2-}	4 Mn^{2+}	8 Fe^{3+}	4 Co^{2+}	4 Zn^{2+}	12 Cu^{2+}
		16 O^{2-}	48 O^{2-}	16 O^{2-}	16 O^2	36 O^{2-}

[a] Closest distance. [b] Longest distance. [c] Most frequent distance.

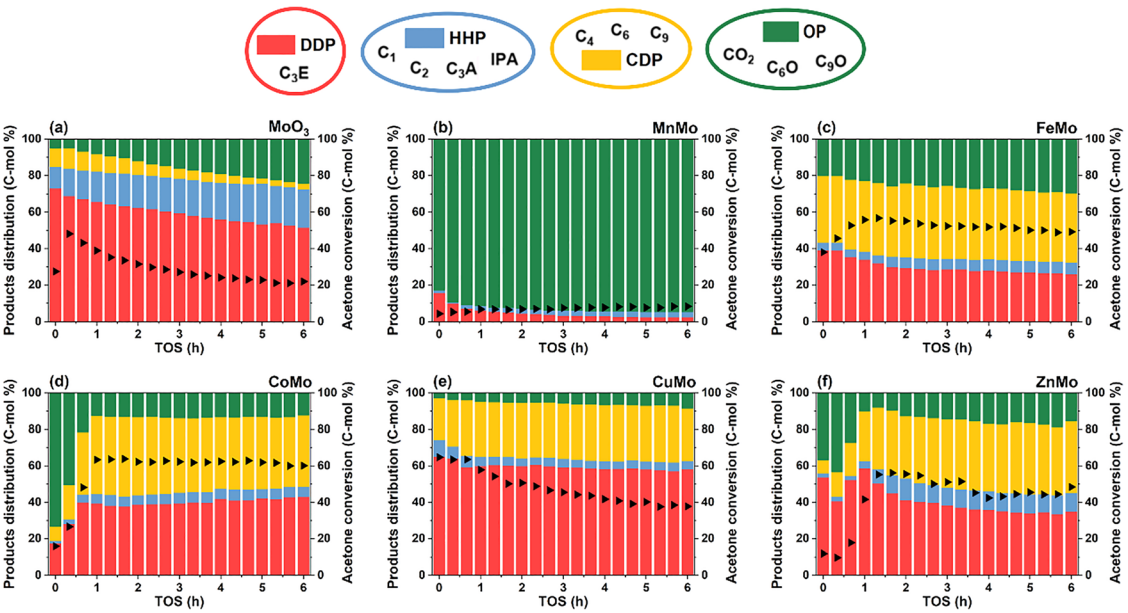

Fig. 2 Products' distribution (colored) and conversion (black triangles) for acetone HDO reaction over (a) MoO_3 and first-row transition metal molybdate catalysts: (b) MnMo, (c) FeMo, (d) CoMo, (e) CuMo, and (f) ZnMo. Isothermal tests were carried out at 400 °C, TOS: 6 h. WHSV = 7.32 $g_{acetone}$ $g_{catalyst}^{-1}$ h^{-1}. Feed: 2.4 mL min^{-1} acetone, 51 mL min^{-1} H_2, balance He. Total flow: 100 mL min^{-1}.

exhibited rapid activation and stable performance, reaching ~60% acetone conversion, corresponding to values of ~60–70 $mmol_{acetone}$ g_{cat}^{-1} h^{-1}, and > 70% of deoxygenated products, with a balanced distribution of DDP and CDP products. This represents an increase of nearly one order of magnitude in acetone consumption rate relative to MnMo. CoMo followed a similar trend; after a brief induction period, it also stabilized at ~60% conversion, reaching the highest sustained acetone consumption rates among the MMo catalysts, ~70–80 $mmol_{acetone}$ g_{cat}^{-1} h^{-1}, and achieved a deoxygenation degree of ~90%. In turn, CuMo achieved its maximum acetone conversion ~60% at the beginning of the reaction, without an induction period, corresponding to approximately 73 $mmol_{acetone}$ g_{cat}^{-1} h^{-1}, and maintained a high deoxygenation degree of ~90% over 6 h, however, a more

© 2026 The Author(s). Published by the Royal Society of Chemistry

Open Access Article. Published on 27 April 2026. Downloaded on 5/21/2026 11:31:09 AM.
This article is licensed under a Creative Commons Attribution-NonCommercial 3.0 Unported Licence.

Table 2 Summary of the catalytic data obtained under acetone HDO isothermal conditions at 400 °C for the first-row transition metal molybdate catalysts: MnMo, FeMo, CoMo, CuMo, and ZnMo. MoO_3 data is presented for comparison

Sample	TOS (h)	Acetone conversion (%)	Acetone consumption rates ($mmol_{acetone}\ g_{cat}^{-1}\ h^{-1}$)	Products' distribution (%)			
				HHP[a]	DDP[a]	CDP[a]	OP[a]
MoO_3	1	39	49	17	65	10	8
	6	22	28	21	51	3	25
MnMo	1	7	9	2	6	—	92
	6	8	10	3	3	—	94
FeMo	1	56	71	4	34	39	23
	6	49	62	7	26	38	29
CoMo	1	63	79	5	39	43	13
	6	60	76	6	42	40	12
CuMo	1	58	73	5	60	30	5
	6	38	48	5	58	29	8
ZnMo	1	55	69	8	50	34	8
	6	48	61	11	35	39	15

[a] HHP: hydrogenation/hydrogenolysis products, DDP: direct deoxygenation products, CDP: coupling deoxygenation products, OP: oxygenation products.

pronounced deactivation was observed as a function of TOS. Despite this deactivation, CuMo remains among the most kinetically active catalysts in the series, and its product distribution remained stable, with DDP accounting for the majority and OP below 10%. As FeMo and CoMo, ZnMo displayed an initial activation period and stabilized at ~50% conversion with ~80% deoxygenation degree and balanced selectivity toward DDP and CDP.

A second series of tests was performed across 300–400 °C. The temperature-dependent profiles further confirmed these trends (Fig. 3 and Table 3, and detailed data in Tables S8–S13). All catalysts exhibited increased conversion with rising temperature, which translated into progressively higher mass-normalized acetone consumption rates, but activation thresholds and selectivity patterns varied. MoO_3 showed minimal activity below 350 °C and limited deoxygenation ability throughout, with acetone consumption rates remaining below ~35 $mmol_{acetone}\ g_{cat}^{-1}\ h^{-1}$, even at 400 °C. MnMo and CoMo also remained largely inactive across the range, operating at similarly low or moderate acetone consumption rates, with OP dominating the product's distribution, confirming their limited site functionality under these conditions. FeMo and ZnMo became catalytically relevant above 360 °C, with a marked increase in conversion and CDP formation at 400 °C, accompanied by a sharp rise in acetone consumption rates to >50 $mmol_{acetone}\ g_{cat}^{-1}\ h^{-1}$, indicative of a transition to kinetically more active regimes. CuMo showed interesting low-temperature performance, achieving 94% conversion and 100% deoxygenation at 300 °C, corresponding to the highest acetone consumption rate

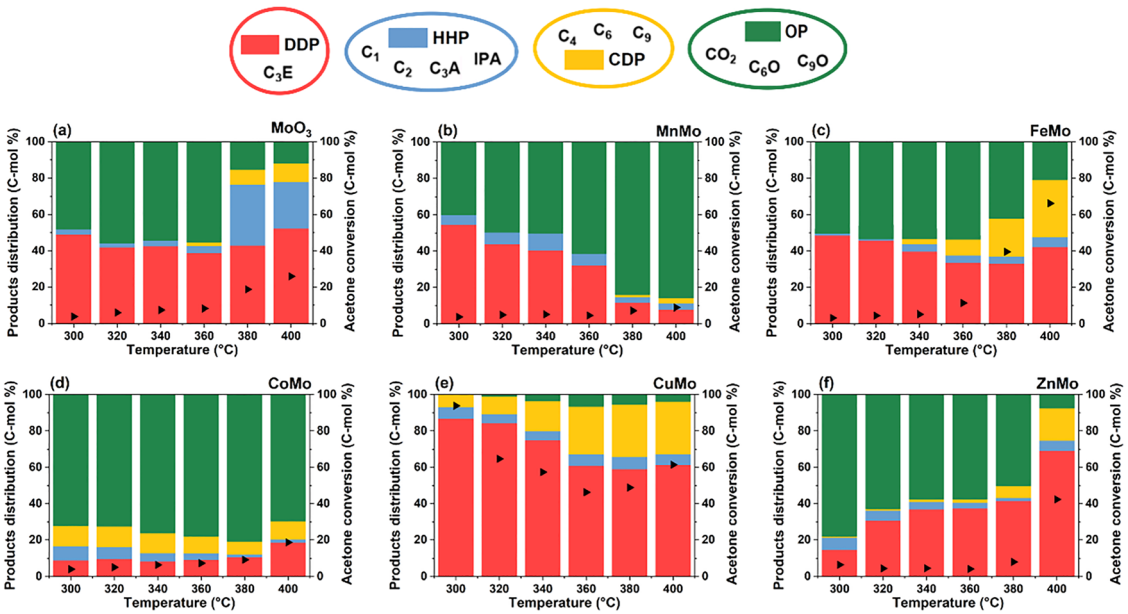

Fig. 3 Products' distribution (colored) and conversion (black triangles) for acetone HDO reaction over (a) MoO_3 and first-row transition metal molybdate catalysts: (b) MnMo, (c) FeMo, (d) CoMo, (e) CuMo, and (f) ZnMo. The temperature-dependent tests were carried out from 300 to 400 °C, isothermal every 20 °C, total TOS: ~3.5 h. WHSV = 7.32 $g_{acetone}\ g_{catalyst}^{-1}\ h^{-1}$. Feed: 2.4 mL min^{-1} acetone, 51 mL min^{-1} H_2, balance He. Total flow: 100 mL min^{-1}.

Open Access Article. Published on 27 April 2026. Downloaded on 5/21/2026 11:31:09 AM. This article is licensed under a Creative Commons Attribution-NonCommercial 3.0 Unported Licence.

Table 3 Summary of the catalytic data obtained for acetone HDO reaction as a function of temperature (300 to 400 °C) for the first-row transition metal molybdate catalysts: MnMo, FeMo, CoMo, CuMo, and ZnMo. MoO_3 data is presented for comparison

Sample	Temperature (°C)	Acetone conversion (%)	Acetone consumption rates ($mmol_{acetone}\ g_{cat}^{-1}\ h^{-1}$)	Products' distribution (%)			
				HHP[a]	DDP[a]	CDP[a]	OP[a]
MoO_3	300	4	5	3	49	—	48
	400	26	33	26	52	10	12
MnMo	300	4	5	6	54	—	40
	400	9	11	4	8	3	85
FeMo	300	3	4	1	49	—	50
	400	66	83	5	42	31	22
CoMo	300	4	5	8	9	11	72
	400	19	24	2	19	10	69
CuMo	300	94	118	6	87	7	—
	400	61	77	6	61	29	4
ZnMo	300	7	9	7	14	1	78
	400	42	53	6	69	18	7

[a] HHP: hydrogenation/hydrogenolysis products, DDP: direct deoxygenation products, CDP: coupling deoxygenation products, OP: oxygenation products.

in the series, ~118 $mmol_{acetone}\ g_{cat}^{-1}\ h^{-1}$, with consistent preference for DDP and CDP over the entire range.

Overall, these results highlight clear structure–function relationships within the MMo series. MoO_3 served as a partially active, single-component reference, characterized by comparatively low reaction rates despite increasing temperature. MnMo remained inert and condensation-selective, while FeMo, CoMo, and ZnMo seemed to undergo restructuring that enables bifunctional HDO behavior, favoring both DDP and CDP and operating at intermediate acetone consumption rates. CuMo emerged as a distinct case, combining low temperature activation and high reactivity, with substantially higher acetone consumption rates than the other systems, and prominent selectivity to DDP at lower temperatures. These performance trends prompted a detailed structural investigation, described in the next section, to correlate catalytic behavior with the post-reaction evolution of each catalyst.

3.2.2. Post-reaction structural, compositional, and surface evolution of MMo catalysts. The acetone HDO reaction at 400 °C induced significant structural, surface, and redox transformations across the MMo catalyst series, as shown in Fig. 4 (XRD, XPS, and TPR data) and Table 4 (surface atomic ratios). A catalyst-by-catalyst analysis revealed distinct transformation pathways and their catalytic implications.

MnMo retained its monoclinic $MnMoO_4$ structure after 6 h on stream, with XRD showing no significant phase transitions (Fig. 4a). This structural robustness correlates with a high fraction of Mo^{6+} (93%) and PM species (7%) observed *via* XPS, suggesting limited reduction (Fig. 4b). TPR analysis revealed no reduction events below 500 °C, in line with manganese's low redox activity under the tested conditions (Fig. 4c). The low surface area (~4 $m^2\ g^{-1}$) and absence of reduced molybdenum species were likely to contribute to its limited HDO performance, where conversion proceeds mainly *via* surface AS, favoring acetone condensation to C_6O.

In turn, FeMo underwent substantial restructuring. XRD revealed the formation of β-MoO_2 (ICSD CollCode 23722) and MoC phases (ICSD CollCode 43523), with no residual Fe-containing crystalline domains. XPS showed partial reduction of Mo^{6+} (down to 77%), accompanied by the formation of Mo^{4+} species (18%), and a significant drop in the Mo/Fe surface ratio (from 3.1 to 1.8), indicating Fe surface exposure. TPR data confirmed that bulk reduction occurs primarily above 500 °C, consistent with the temperature required for the collapse of the MMo framework. The formation of MoC rather than β-Mo_2C suggests a transformation pathway triggered by acetone HDO conditions, which is different than conventional carburization. This is notable given that most literature emphasizes β-Mo_2C as the thermodynamically favored carbide and the main active phase in HDO.[51] While β-Mo_2C is efficient for C–O bond scission, it requires surface oxygen enrichment to enable bifunctional reactivity.[41]

CoMo exhibited a similar transformation pathway. XRD also indicated formation of β-MoO_2 and MoC, with no detectable cobalt crystalline phases. The XPS analysis revealed a decline in Mo^{6+} content (down to 59%), with oxide Mo^{4+} species emerging to 29%, and the Mo/Co surface ratio falling from 1.7 to 0.9, suggesting a metal migration to the surface during restructuring. These changes are consistent with prior reports of $CoMoO_4$ transformation under reducing and carburizing conditions. Rodriguez *et al.* showed that $CoMoO_4$ undergoes sequential reduction to $Co_2Mo_3O_8$ and $CoMoO_3$ under H_2,[52] while Xu *et al.* demonstrated that under CH_4/H_2 atmospheres, $CoMoO_4$ evolves into CoO at 490 °C, followed by MoC + Co^0 at 720 °C, and finally β-Mo_2C + Co^0 at 760 °C.[29] Although the acetone HDO stream promotes phase transitions at lower temperature and in the absence of conventional carburizing agents, the formation of MoC (instead of β-Mo_2C) and likely-amorphous CoO_x or Co^0 domains suggest a kinetically driven collapse of the $CoMoO_4$ lattice.

CuMo displayed the most pronounced restructuring. Post-reaction XRD detected only crystalline Cu^0 (ICSD collcode 7954), with complete disappearance of molybdenum-based crystalline phases. XPS showed a sharp drop in surface Mo/Cu from 1.1 to 0.6, with the formation of Mo^{4+} species (16%). TPR revealed low-temperature reduction peaks at 327 °C and

© 2026 The Author(s). Published by the Royal Society of Chemistry

Open Access Article. Published on 27 April 2026. Downloaded on 5/21/2026 11:31:09 AM.
This article is licensed under a Creative Commons Attribution-NonCommercial 3.0 Unported Licence.

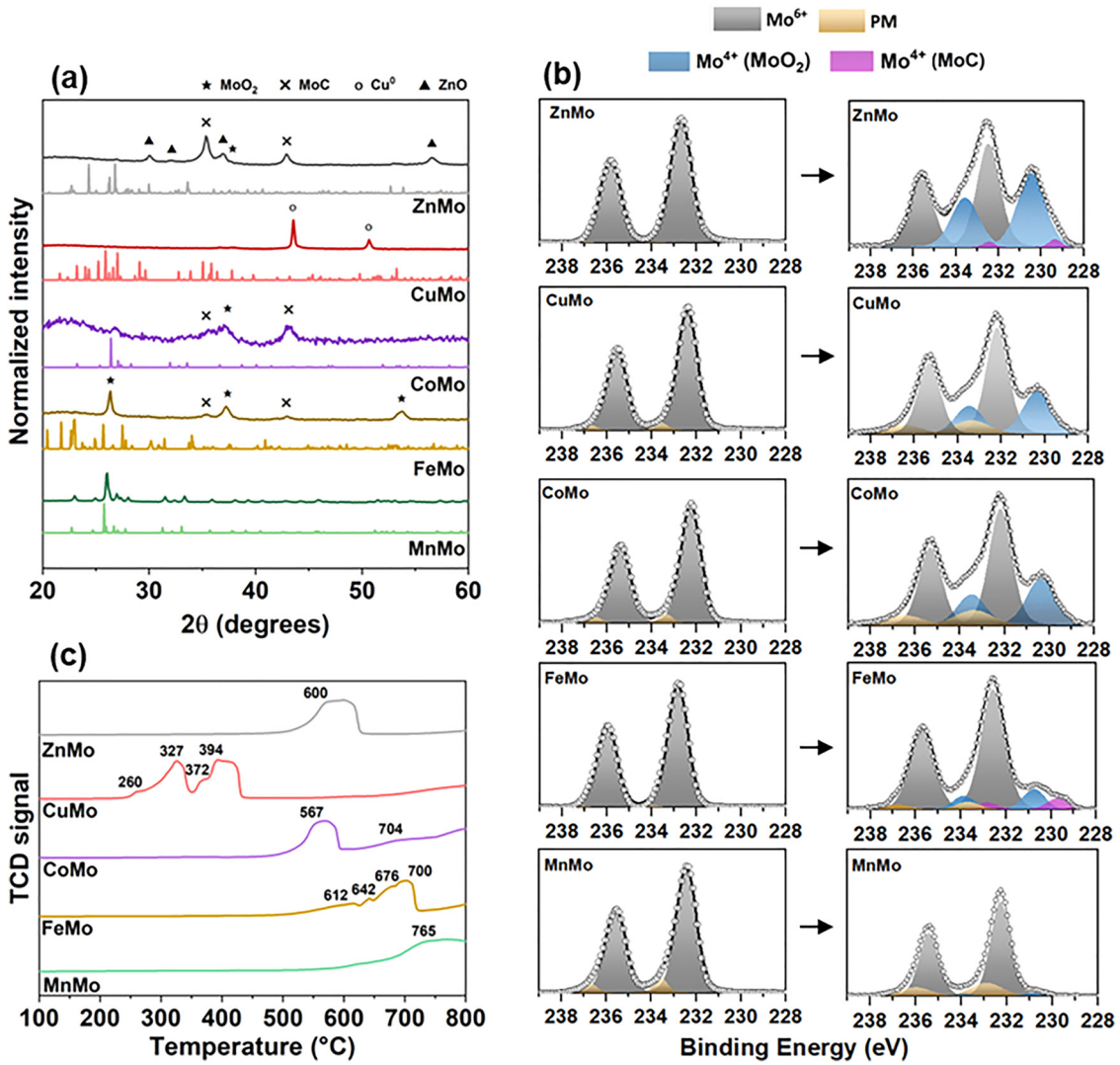

Fig. 4 Structural, surface, and redox characterization of fresh and post-reaction (400 °C, isothermal) first-row metal molybdate catalysts (MMo): MnMo, FeMo, CoMo, CuMo, and ZnMo. (a) Powder XRD patterns collected after catalytic reaction (dark colored) and the corresponding simulated patterns (light colored) obtained from the ICSD collection.[45] Other phases were indicated by graphical symbols: MoO_2 (★), MoC (×), Cu^0 (○), and ZnO (▲). (b) XPS spectra of the fresh (left) and post-reaction catalysts (right); PM corresponds to the polymolybdates species. (c) H_2-TPR profiles of fresh catalysts under 5% H_2/Ar flow up to 800 °C.

Table 4 Atomic surface ratios and species for fresh and post-reaction (isothermal, 400 °C) MMo catalysts. Nominal values are based on precursor stoichiometry

Sample	Nominal Mo/M ratios	Atomic surface Mo/M ratios[a]		Surface atomic Mo species ratios[a] PM : Mo^{6+} : Mo^{4+}	
		Fresh	Post-reaction	Fresh	Post-reaction
MnMo	1.0	2.1	1.1	0.07 : 0.93 : 0.00	0.19 : 0.78 : 0.03
FeMo	1.5	3.1	1.8	0.01 : 0.99 : 0.00	0.05 : 0.77 : 0.18
CoMo	1.0	1.7	0.9	0.05 : 0.95 : 0.00	0.12 : 0.59 : 0.29
CuMo	0.7	1.1	0.6	0.04 : 0.96 : 0.00	0.14 : 0.70 : 0.16
ZnMo	1.0	1.5	1.1	0.00 : 1.00 : 0.00	0.00 : 0.53 : 0.47

[a] Obtained through XPS analysis: more details in Tables S14 and S15.

394 °C, corresponding to $Cu^{2+} \rightarrow Cu^{+}$ and $Cu^{+} \rightarrow Cu^{0}$, respectively, significantly lower than those of other MMo catalysts. These results confirmed CuMo's high reducibility and structural instability under HDO conditions. According to Xu *et al.*,[29] when $CuMoO_4$ is submitted to CH_4/H_2, it yields Cu^0 above 240 °C, with MoO_xC_y, Mo^0, and β-Mo_2C forming sequentially upon further heating. Although such β-Mo_2C formation was not observed here, the data suggest molybdenum became amorphous, likely as MoO_x and/or MoO_xC_y. The resulting dual structure, composed of Cu^0 and amorphous molybdenum species, correlates with CuMo's HDO performance: high initial conversion (58%), stable activity after 6 h, and high deoxygenation degree (>90%). These features echo observations in CO_2 hydrogenation studies, where Cu/Mo_2C exhibited high selectivity towards methanol,[29] highlighting the potential of Cu-Mo bifunctional systems.

Finally, ZnMo underwent moderate restructuring. As post-reaction FeMo and CoMo, XRD patterns showed formation of

Open Access Article. Published on 27 April 2026. Downloaded on 5/21/2026 11:31:09 AM.
This article is licensed under a Creative Commons Attribution-NonCommercial 3.0 Unported Licence.

β-MoO_2 and MoC, alongside a minor segregated ZnO phase (ICSD CollCode 26170). Surface XPS revealed the most reduced Mo content, with 53% of Mo^{6+}, the emergence of Mo^{4+} species (47%), and surface Mo/Zn ratio drop from 1.5 to 1.1. TPR analysis showed ZnMo's reducibility to be also comparable to FeMo and CoMo, with significant reduction beginning only above 500 °C. The functional difference commonly attributed to Fe, Co, and Zn catalysts, together with the predominant presence of more reduced molybdenum phases and the similar catalytic activity observed, indicated that these molybdenum phases, acting synergistically, are the main responsible for the HDO activity and the promotion of CDP.

Across the series, insights from the literature highlight the divergence between conventional carburizing pathways (CH_4/H_2) and the mechanisms active during acetone HDO. While β-Mo_2C formation typically occurs at higher temperatures and under carburizing atmospheres,[29] our data indicate that MoC formation and MoO_xC_y amorphization dominate under HDO conditions. This distinction is critical, as MoC and amorphous Mo^{4+} phases, though less thermodynamically stable, still provide active sites for C═O activation and deoxygenation. Furthermore, while MoO_3 is traditionally considered more catalytically active than MoO_2, its superior performance is often linked to the dynamic formation of substoichiometric domains such as MoO_xC_y, which offer both redox and acid functionalities.[53,54] In contrast, MoO_2 is less reactive and more structurally inert. Our previous work demonstrated that MoO_2 primarily yields IPA and C_6O, with minimal deoxygenation activity,[9] consistent with its inability to form bifunctional surfaces under mild reduction.

Interestingly, the post-reaction XPS data in Table 4 revealed that the surface Mo/M ratios across all catalysts tend to converge toward their respective nominal stoichiometric values, in contrast to the significant surface Mo enrichment observed in the fresh materials. This convergence suggests that the initially segregated MoO_x-rich outer layers, likely composed of polymolybdate-like domains, are no longer structurally or functionally distinct after reaction. Under the reducing and carburizing environment of acetone HDO at 400 °C, these surface domains are likely incorporated into a more complex mixture of phases. The evolution toward a more homogenized and stoichiometrically consistent surface reflects the dynamic restructuring of the catalyst, where the former surface MoO_x-enrichment becomes functionally irrelevant.

Collectively, these findings confirm that the acetone HDO reaction at 400 °C induced distinct transformation routes for each MMo catalyst: MnMo remained intact and inactive; FeMo, CoMo, and ZnMo restructured into reduced MoC/MoO_2-rich phases with amorphous domains; CuMo collapsed into a Cu^0/amorphous MoO_xC_y system. Catalytic activity correlates with the generation of Mo^{4+} and dynamic surface restructuring, emphasizing the importance of redox-active molybdenum species and the role of transition metal synergy in driving selective HDO under reaction conditions.

3.3. Unravelling CuMo catalyst evolution under acetone HDO

3.3.1. HDO performance of CuMo across extended temperatures. Among the MMo catalysts, CuMo displayed a distinctive catalytic profile, marked by high HDO activity and deoxygenation even at relatively low temperatures. To investigate the origin of this behavior, we conducted a temperature-dependent catalytic study of CuMo displayed in Fig. 5 and Table 5 (see also Table S16). At 100–200 °C, CuMo promoted the formation of HHP and DDP despite low acetone conversion (6–7%), corresponding to low acetone consumption rates, ~8–9 $mmol_{acetone}\ g_{cat}^{-1}\ h^{-1}$. A sharp performance enhancement was observed at 250 °C, with conversion reaching 81% and total deoxygenation. The product distribution markedly shifted toward DDP 84% and CDP 10%. At 300 °C, conversion and selectivity remained stable, with DDP and CDP jointly accounting for 96% of the products. In both temperatures, the acetone consumption rate showed a 10-fold increase, to ~100 $mmol_{acetone}\ g_{cat}^{-1}\ h^{-1}$, highlighting the transition to a kinetically dominant deoxygenation regime, and indicating that the active sites responsible for deoxygenation are already available by 250 °C.

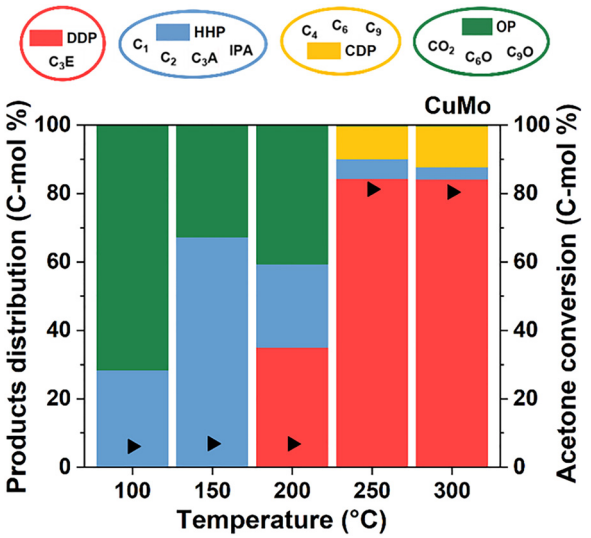

Fig. 5 Products' distribution (colored) and conversion (black triangles) for acetone HDO reaction over CuMo catalyst. The temperature-dependent isothermal test was carried out from 100 to 300 °C, total TOS: ~3 h. WHSV = 7.32 $g_{acetone}\ g_{catalyst}^{-1}\ h^{-1}$. Feed: 2.4 mL min^{-1} acetone, 51 mL min^{-1} H_2, balance He. Total flow: 100 mL min^{-1}.

To understand the structural basis for the low temperature activation, we refer back to the post-reaction analysis presented in Section 3.2, which showed that CuMo underwent a pronounced structural transformation under HDO conditions. At 400 °C, only crystalline Cu^0 was detected, with no trace of crystalline molybdenum phases (Fig. 4 and Fig. S2), indicating that molybdenum transitions into an amorphous state. This restructuring is attributed to the high reducibility of copper, which destabilizes the $Cu_3Mo_2O_9$ lattice and promotes the formation of a disordered MoO_xC_y-rich domain. The emergence of this bifunctional architecture, combining metallic copper with active amorphous molybdenum domains, supports the catalyst's ability to promote deoxygenation reactions even at relatively low temperatures.

To assess whether this synergy results from intrinsic Cu–Mo interaction or could be replicated in simpler systems, we tested

© 2026 The Author(s). Published by the Royal Society of Chemistry

Open Access Article. Published on 27 April 2026. Downloaded on 5/21/2026 11:31:09 AM. This article is licensed under a Creative Commons Attribution-NonCommercial 3.0 Unported Licence.

Table 5 Summary of the catalytic data obtained for acetone HDO reaction as a function of temperature (100 to 300 °C) for the CuMo catalyst

Sample	Temperature (°C)	Acetone conversion (%)	Acetone consumption rates ($mmol_{acetone}\ g_{cat}^{-1}\ h^{-1}$)	Products' distribution (%)			
				HHP[a]	DDP[a]	CDP[a]	OP[a]
CuMo	100	6	8	28	0	0	72
	150	7	9	67	0	0	33
	200	7	9	24	35	0	41
	250	81	102	6	84	10	0
	300	80	100	4	84	12	0

[a] HHP: hydrogenation/hydrogenolysis products, DDP: direct deoxygenation products, CDP: coupling deoxygenation products, OP: oxygenation products.

single-component and physically mixed catalysts (Fig. S3 and Table S17, with detailed data in Tables S18–S21). Neither CuO nor Cu_2O alone was active: both showed poor conversion (8% and 4%) and predominantly yielded IPA, corresponding to very low acetone consumption rates under fixed feed composition and WHSV. A physical mixture of CuO and MoO_3 (3Cu:2Mo) increased conversion (21%) and promoted high deoxygenation (99%), yet operated at substantially lower reaction rates than CuMo, but the limited interfacial contact likely restricted the formation of truly synergistic sites. Similarly, the impregnated CuO/MoO_3 sample (10 wt% Cu) produced only 8% conversion with broader selectivity (15% CDP, 39% OP), underscoring that copper loading and contact alone did not replicate the CuMo behavior. These results reinforce that CuMo's performance should arise from its structural integration and dynamic phase evolution under reaction conditions.

To further probe the origin of CuMo's performance, comparative experiments were conducted with both fresh MoO_3 and a pre-treated MoO_3 sample. The latter was subjected to acetone HDO at 400 °C for 30 min to promote partial carburization and the formation of MoO_xC_y/MoO_2 phases prior to testing. As shown in Fig. S4 and Table S22, the fresh MoO_3 exhibited minimal activity up to 300 °C, with only 5% conversion, corresponding to low acetone consumption rates across the entire temperature range, and product distributions dominated by DDP, probably related to OVS alongside trace amounts of CDP and OP.[9] In contrast, the pre-treated MoO_3 initially favored OP with a small 4% conversion. Up to 300 °C, the conversion increased to 18%, reflecting a moderate increase in acetone consumption rate but remaining well below that of CuMo, with a shift in product selectivity favoring DDP (44%). These changes were consistent with the formation of MoO_xC_y domains, previously shown to enhance Brønsted acidity and hydrogenating capability under HDO conditions.[9]

Despite this improvement, pre-treated MoO_3 still underperformed relative to CuMo, both in conversion and product selectivity. These results highlighted that while MoO_xC_y domains contributed with important functionalities, including stronger BAS and undercoordinated species, they did not fully account for CuMo's distinct catalytic behavior. Instead, our findings indicate that the copper–molybdenum interaction during *in situ* restructuring played a decisive role.

Taken together, these observations suggest that CuMo's HDO performance arises from a dynamic synergy between copper and molybdenum species. Copper likely acts as a structural destabilizer, triggering the collapse of the $Cu_3Mo_2O_9$ framework at moderate temperatures and promoting the early emergence of an amorphous Mo-rich surface. This disordered MoO_xC_y phase coexisted with metallic copper.

To gain further insight into the structural and chemical dynamics underlying this behavior, a more detailed characterization of the CuMo catalyst was performed. To capture surface changes and correlate them with product's distribution, *ex situ* techniques and *operando* DRIFTS were additionally performed in CuMo exposed to reaction conditions at different temperatures (175, 200, and 300 °C).

3.3.2. Structural and surface dynamics of CuMo under reaction conditions. The stepwise structural evolution of CuMo under acetone HDO conditions was captured by XRD measurements as a function of temperature, as displayed in Fig. 6a. The fresh catalyst displays well-defined peaks associated with orthorhombic $Cu_3Mo_2O_9$, with a mean crystallite size of ~77 nm. Upon exposure to acetone HDO conditions at 175 °C, these reflections diminish markedly and new peaks corresponding to metallic Cu^0 (50 nm) and MoC (29 nm) emerged, indicating the onset of molybdate reduction and initial carburization. At 200 °C, Cu^0 peaks increase in intensity while MoC reflections faded, disappearing entirely at 300 °C. At this point, only Cu^0 remained detectable (46 nm), suggesting complete amorphization or high dispersion of molybdenum, likely as substoichiometric MoO_xC_y. This phase was inferred in our previous work on MoO_3 exposed to acetone HDO reaction stream.[9]

An in-depth structural analysis of the short- to medium-range order was conducted by PDF analysis, which provides real-space structural information derived from both Bragg and diffuse scattering contributions. The real-space Rietveld refinement of the short-range order [1.5–10 Å] of post-reaction CuMo at 300 °C is shown in Fig. 6b, whereas the data for the fresh and post-reaction at 200 °C samples were shown in Fig. S5a–d. The gray open circles represent the experimental data, the red solid line the calculated data, and the gray solid line the residual curve. Fresh CuMo refinements align with the XRD data, in which the experimental PDFs were well described against the crystalline $Cu_3Mo_2O_9$ model. On the other hand, Fig. 6b confirmed that Cu^0 motifs dominate the experimental PDF of the CuMo exposed to 300 °C under HDO reaction conditions, as highlighted by the goodness of the fit (*i.e.*, R_w) against a Cu fcc

Open Access Article. Published on 27 April 2026. Downloaded on 5/21/2026 11:31:09 AM.
This article is licensed under a Creative Commons Attribution-NonCommercial 3.0 Unported Licence.

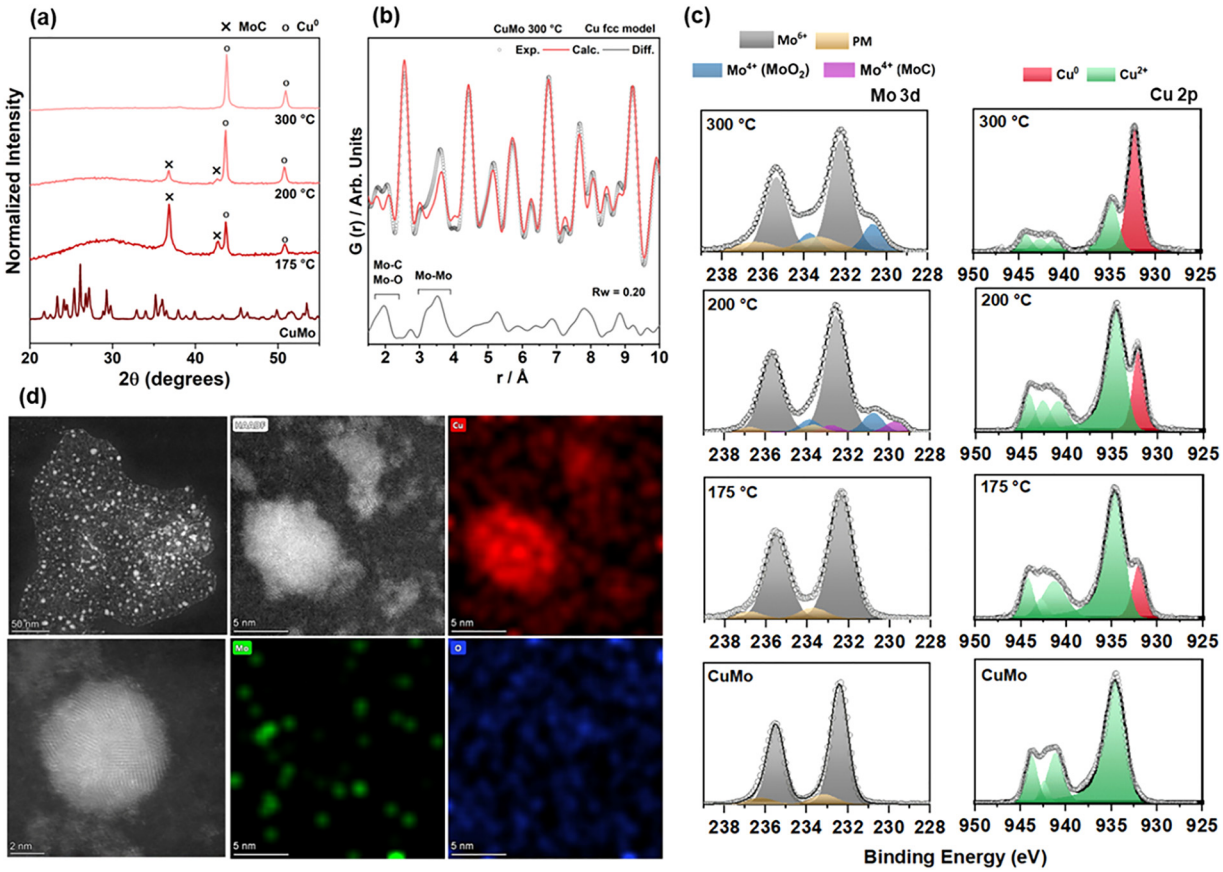

Fig. 6 Structural and morphological evolution of the CuMo catalyst under acetone HDO conditions. (a) XRD patterns of the fresh CuMo and post-reaction samples treated at 175, 200, and 300 °C for 1 h. (b) PDF refinement of the post-reaction CuMo sample at 300 °C fitted to an fcc Cu model, evidencing the short-range metallic ordering. (c) Mo 3d (left) and Cu 2p (right) XPS spectra of the CuMo catalysts after reaction. (d) HAADF-STEM image, high-resolution TEM, and corresponding EDX elemental maps (Cu = red, Mo = green, O = blue) of the CuMo catalyst treated at 300 °C.

model of 0.20. The difference curve PDF revealed residual Mo–C/Mo–O and Mo–Mo motifs, likely associated with a molybdenum (oxy)carbidic phase.[9] Finally, a combination of crystalline $Cu_3Mo_2O_9$ and MoC motifs could partially describe the short-range order of CuMo exposed to reaction conditions at 200 °C (Figure S5c) (R_w = 0.38), with $Cu_3Mo_2O_9$ representing *ca.* 91% of the atomic phase fraction.

The difference curve highlights the presence of peaks agreeing with Cu–Cu pairs at 2.7 Å, associated with the Cu fcc crystalline domains observed in the XRD data. Peaks from residual amorphous molybdenum (oxy)carbidic phases can also be seen at 1.5–2.2 Å (Mo–O/Mo–C) and 3.0–3.9 Å (Mo–Mo). These attributions are consistent with Mo–O/Mo–C and Mo–Mo distances observed in molybdenum oxides and carbides (Fig. S6a and b). Compared to the fresh CuMo, an increase in the atomic displacement parameter values (2.3-, 3-, and 5.5-fold for Cu, Mo, and O, respectively) and notable expansion of the *a*-lattice (16%) and contraction of the *c*-lattice (7%) parameters (Table S24) were observed for the $Cu_3Mo_2O_9$ phase. These structural modifications are consistent with the destabilization of the $Cu_3Mo_2O_9$ lattice caused by copper migration and partial depletion, leading to the formation of highly disordered nanodomains that are only locally described within r distances below 10 Å. On the other hand, the medium-range order (Fig. S5d) was well described (R_w = 0.25) by a model comprising MoC (95%) and Cu (5%). These structural insights indicate that at intermediate temperatures (*i.e.*, 200 °C), the formation of a fraction of MoC and partial exsolution of copper occur. Simultaneously, the crystalline $Cu_3Mo_2O_9$ phase evolves to a highly distorted $Cu_3Mo_2O_9$ phase with local structural motifs (<10 Å), retaining copper in its structure. Exposing the catalyst to reaction conditions at 300 °C, these local $Cu_3Mo_2O_9$ motifs collapsed by the exsolution of the remaining copper, resulting in a system composed of Cu^0 and amorphous molybdenum (oxy)carbidic phases.

This dual phase model is further supported by TEM-EDX analysis presented at Fig. 6d. The HAADF-STEM images show irregular nanoparticles (~5 nm) with a denser matrix supported on an extremely thin layer of a less dense material, as evidenced by the image contrast. Elemental mapping by EDX (spectrum in Fig. S7) confirms that the denser particles are copper-rich, while the thin support contains Mo, O, and also Cu. These observations strongly support the phase segregation model inferred from XRD and PDF, where crystalline Cu^0 nanoparticles are embedded in a disordered MoO_x/MoO_xC_y matrix. Larger copper particles (<50 nm) are also

© 2026 The Author(s). Published by the Royal Society of Chemistry

Open Access Article. Published on 27 April 2026. Downloaded on 5/21/2026 11:31:09 AM.
This article is licensed under a Creative Commons Attribution-NonCommercial 3.0 Unported Licence.

Table 6 Bulk and surface atomic Mo/Cu ratios and relative surface species of the fresh and post-reaction CuMo catalysts. XRF analysis reflects bulk composition, whereas XPS reveals the surface elemental ratios

CuMo catalysts	Atomic Mo/Cu ratios		Atomic surface species ratios[b]	
	Bulk[a]	Surface[b]	PM : Mo^{6+} : Mo^{4+}	Cu^{2+} : Cu^0
Fresh	0.9	1.1	0.04 : 0.96 : 0.00	1.00 : 0.00
175 °C	0.6	0.4	0.10 : 0.90 : 0.00	0.87 : 0.13
200 °C	0.5	0.6	0.06 : 0.92 : 0.04	0.81 : 0.19
300 °C	0.5	1.2	0.17 : 0.68 : 0.15	0.46 : 0.54

[a] Obtained through XRF analysis. [b] Obtained through XPS analysis: more details in Table S23.

seen (Fig. S8), justifying the crystallite size (46 nm) observed by XRD.

XPS analysis displayed in Table 6 (see also Table S23) revealed the redox evolution of surface species throughout this transformation. Between 175 °C and 200 °C, the surface was dominated by Mo^{6+} (>93%), with negligible Mo^{4+} content and a $Cu^{2+}/Cu^{0/1+}$ ratio between 6 and 4. This redox configuration was consistent with the stability of the $Cu_3Mo_2O_9$ phase and the formation of minor reduced copper phases. By 300 °C, an increase in Mo^{4+} species was observed (15%), standing close to the 14% observed for the catalyst spent at 400 °C, shown in the previous section. Cu^0 accounts for 54% of the surface copper, the maximum between the different reaction temperatures. The surface Mo/Cu ratio increased from 0.6 at 200 °C to 1.2 at 300 °C, while the bulk ratio remained around 0.5. This enrichment confirms that molybdenum became preferentially localized at the surface in its disordered, amorphous form, while copper segregated both as nanoparticles and larger crystalline particles.

Operando DRIFTS measurements provide dynamic insight into the surface evolution of CuMo under HDO conditions. As shown in Fig. 7, at 175 °C, vibrational features in the low wavenumber region (Fig. 7b) revealed surface-bound polymolybdate species: bands between 1000–900 cm^{-1} are attributed to Mo=O terminal stretching (νMo=O), while those between 900–500 cm^{-1} correspond to Mo–O–Mo bridging modes (νMo–O–Mo).[55] These signals were consistent with a surface enriched in polymolybdate domains, as previously inferred from XPS analysis. Characteristic bands of the $Cu_3Mo_2O_9$ lattice, particularly at 960, 932, 832, and 811 cm^{-1},[56–60] were absent, suggesting that the crystalline molybdate framework was either coated or structurally disrupted at the surface.

After 1 h on stream at 175 °C, these polymolybdate-related bands vanished completely, indicating rapid surface decomposition or transformation under reaction conditions. Concurrently, in the high wavenumber region (Fig. 7a), the hydroxyl stretching bands at 3440 and 3355 cm^{-1} decreased sharply, pointing to significant surface dehydroxylation and the partial loss of BAS.

These spectroscopic changes were mirrored by a simultaneous increase in C_3E (DDP) and C_6O (OP) formation (Fig. 7c), reflecting a sharp onset in deoxygenation activity. Given the concurrent disappearance of surface –OH groups and the rise in deoxygenated products, it is unlikely that classical surface Brønsted hydroxyl groups were the primary contributor to this reactivity. Importantly, copper-related vibrations were absent from the DRIFTS data, likely due to rapid exsolution and localization within subsurface crystallites. Rather, the data point to the formation of a new catalytically active surface phase, most likely the proposed disordered MoO_xC_y domains.

Together, these observations confirm that CuMo underwent a profound structural and chemical transformation beginning at temperatures as low as 175–200 °C. The initial orthorhombic $Cu_3Mo_2O_9$ phase collapsed *via* Cu^{2+} reduction and exsolution, leading to transient formation of MoC and a subsequent redistribution of molybdenum into a disordered, enriched MoO_xC_y domain. The resulting composite, crystalline Cu^0 domains embedded in an amorphous molybdenum oxycarbide network, emerged as the catalytically active phase under HDO conditions.

This Cu^0/MoO_xC_y system seems to exhibit a dynamically bifunctional catalytic character. Metallic Cu^0 facilitates hydrogenation and H-transfer reactions, while the substoichiometric molybdenum species offer a versatile landscape of redox-active sites and acid sites. XPS and DRIFTS data revealed a pronounced

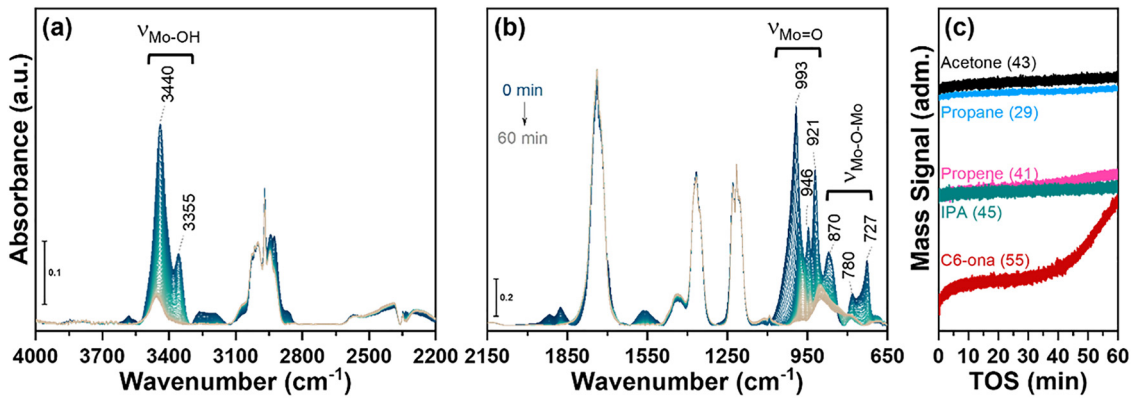

Fig. 7 *Operando* DRIFTS of CuMo highlighting the (a) high-wavenumber region, (b) low-wavenumber region, (c) results from mass spectrometry. WHSV = 3.66 $g_{acetone}$ $g_{catalyst}^{-1}$ h^{-1}. Feed: 2.1 mL min^{-1} acetone, 44 mL min^{-1} H_2, balance He. Total flow: 50 mL min^{-1}.

Open Access Article. Published on 27 April 2026. Downloaded on 5/21/2026 11:31:09 AM.
This article is licensed under a Creative Commons Attribution-NonCommercial 3.0 Unported Licence.

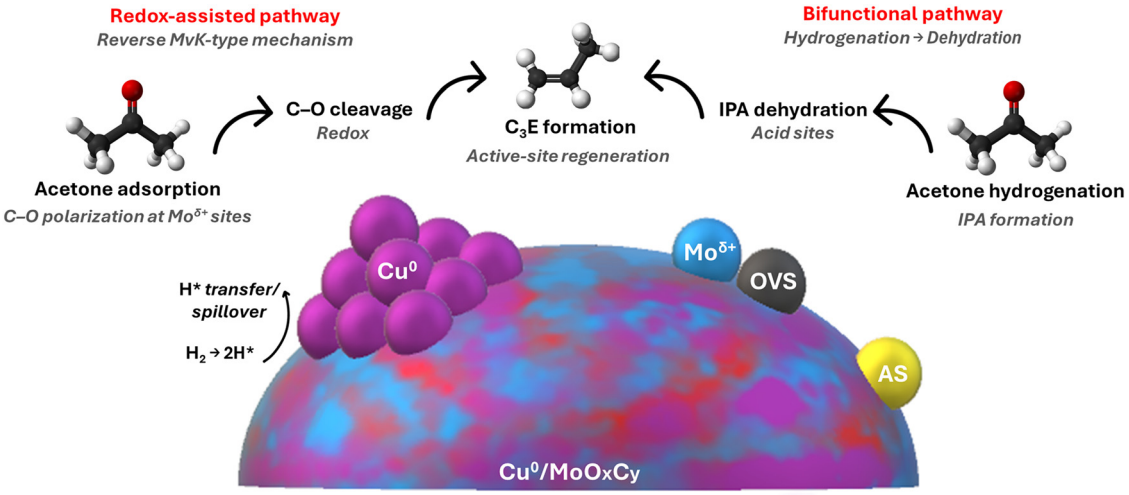

Scheme 3 Proposed mechanistic picture for acetone deoxygenation over Cu^0/MoO_xC_y under HDO conditions. Partial carburization and reduction generate disordered MoO_xC_y domains enriched in oxygen vacancies (OVS), coordinatively unsaturated $Mo^{\delta+}$ sites (mixed oxidation states $Mo^{6+}/Mo^{5+}/Mo^{4+}$), and acidic functionalities (AS). Acetone adsorption and C═O polarization occur at $Mo^{\delta+}$ sites, enabling a redox-assisted C–O cleavage pathway (reverse MvK-type) followed by active-site regeneration. A bifunctional route involving Cu^0-assisted hydrogenation to IPA and subsequent dehydration on acid sites also leads to C_3E formation.

surface enrichment in molybdenum and a decline in Brønsted acidity upon dehydroxylation, suggesting that the catalytic mechanism is predominantly governed by redox and Lewis acid pathways. Together with TEM-EDX mapping, the absence of copper signatures in DRIFTS supports the view that copper's role is structural and electronic in promoting molybdate destabilization and electronic restructuring, rather than direct participation in adsorption or activation of oxygenates.

Remarkably, this restructuring initiates around 175 °C, where, as evidenced by comparative MoO_3 studies, OVS and AS dominate catalysis, favoring pathways such as direct deoxygenation and condensation.[9] At elevated temperatures (≥300 °C), the emergence of HS becomes increasingly relevant, giving rise to more diverse deoxygenation products. In CuMo, this transition is accelerated and intensified by the presence of copper, which not only facilitates molybdenum reduction but also promotes the formation of a disordered surface rich in undercoordinated $Mo^{\delta+}$ species and OVS, conditions that support cooperative and bifunctional reactivity.

Building on the combined structural, spectroscopic, and catalytic evidence, a plausible mechanistic picture can be proposed for the role of Cu^0/MoO_xC_y in promoting high acetone deoxygenation, as depicted in Scheme 3. The partial carburization and reduction of molybdenum oxides under reaction conditions generates disordered MoO_xC_y surfaces characterized by a high density of oxygen vacancies, mixed Mo oxidation states ($Mo^{6+}/Mo^{5+}/Mo^{4+}$), and the emergence of strong, non-classical acidic functionalities. Given prior knowledge and extensive literature on MoO_3 and related molybdenum-based systems under HDO conditions,[9,35,41,54,61–67] acetone adsorption is favored at coordinatively unsaturated $Mo^{\delta+}$ sites, where the C═O group can be activated through metal–oxygen interactions. Subsequent C–O bond cleavage can proceed *via* a redox-assisted pathway analogous to a reverse MvK mechanism. At more advanced stages of restructuring and at higher temperatures, the reorganization of surface oxygen species and acidic functionalities on MoO_xC_y facilitate dehydration pathways, enabling C_3E formation either directly from activated acetone or *via* IPA intermediates. The coexistence of redox-active molybdenum centers and strong Brønsted acidity within the same disordered MoO_xC_y domains thus provides a bifunctional environment that favors deoxygenation while limiting unselective hydrogenation. In Cu^0/MoO_xC_y systems, subsurface or segregated copper species may further assist hydrogen activation and H-transfer, enhancing the redox cycling of molybdenum sites without compromising the acidic functionality of the oxycarbide surface.

In contrast to MnMo, FeMo, CoMo, and ZnMo, where the transition metal primarily governs the extent and temperature of molybdate restructuring but does not introduce clear and distinct catalytic functionalities, CuMo displays a fundamentally different behavior. Its superior HDO performance arises from a spontaneous, low-temperature transformation into a Cu^0/MoO_xC_y composite. This functional domain forms through a unique sequence of copper exsolution, molybdate collapse, and redistribution into a catalytically active, surface-enriched matrix. The synergy between dispersed Cu^0 domains and reduced molybdenum species provides a platform for multifaceted activation modes, including condensation, deoxygenation, and hydrogenation, setting CuMo apart from the other MMo systems and Cu-related catalysts in both activity and selectivity.[68–77]

4. Conclusions

This study provides an insightful understanding of how first-row transition metal molybdates evolve under HDO conditions

© 2026 The Author(s). Published by the Royal Society of Chemistry

Open Access Article. Published on 27 April 2026. Downloaded on 5/21/2026 11:31:09 AM. This article is licensed under a Creative Commons Attribution-NonCommercial 3.0 Unported Licence.

and how their structural dynamics influence the catalytic performance. Through a systematic investigation combining catalytic evaluation, *ex situ* and *operando* characterizations, and structural analysis, we demonstrate that the acetone HDO environment drove distinct restructuring pathways across the MMo catalyst series (Mn, Fe, Co, Cu, Zn). These pathways range from structural stability and inactivity (MnMo) to extensive reduction, carburization, and surface amorphization (FeMo, CoMo, ZnMo), with CuMo exhibiting a unique low-temperature transformation into a bifunctional Cu^0/amorphous MoO_xC_y system. While acetone was employed here as a representative probe molecule, its ability to engage redox, acidic, and hydrogenation pathways makes it particularly suitable for elucidating restructuring-driven catalytic functionality, which is expected to be broadly relevant to other oxygenated substrates under HDO conditions.

The findings highlight the central role of active reduced molybdenum species in enabling effective C–O bond cleavage and selective deoxygenation. The synergistic interplay between molybdenum and the transition metal, especially copper, emerged as a key factor in tuning the onset temperature, product distribution, and deactivation resistance of the catalyst. The integration of *operando* DRIFTS and real-space structural probes such as PDF provided crucial evidence for the formation of dynamic, catalytically relevant phases.

This study improves our understanding of how molybdate catalysts behave and evolve under reaction conditions, and points toward more intentional strategies for catalyst design. We show that these materials can reorganize into active, bifunctional structures *in situ*, which may be used as a design principle in future systems. In particular, Cu–Mo catalysts appear to be promising platforms for studies involving cooperative catalysis, redox control, and selective biomass conversion. Continued work exploring other metal–molybdenum combinations, phase evolution, and *in situ* characterization will be important to expand these ideas to more complex feedstocks and reaction environments.

Author contributions

Gabriel B. Báfero: conceptualization, investigation, methodology, visualization, writing – original draft, writing – review and editing. Guilherme B. Strapasson: investigation, methodology, visualization, writing – original draft. Leonardo S. Sousa: investigation, methodology, visualization, writing – original draft. James S. Hayward: methodology. Pedro B. M. Nunes: methodology, visualization, writing – original draft. Davi S. Leite: methodology, visualization, writing – original draft. David J. Morgan: methodology, visualization, writing – original draft. Jonathan K. Bartley: conceptualization, methodology, funding acquisition, project administration, supervision, writing – original draft. Daniela Zanchet: conceptualization, methodology, visualization, funding acquisition, project administration, supervision, writing – original draft, writing – review and editing.

Conflicts of interest

The authors declare that they have no known competing financial interests or personal relationships that could have appeared to influence the work reported here.

Data availability

All processed data are provided in the main article and supplementary information (SI). Raw datasets are available from the corresponding author upon reasonable request.

Supplementary information is available. See DOI: https://doi.org/10.1039/d5ey00359h.

Acknowledgements

This work was funded in part by the Fundação de Amparo à Pesquisa do Estado de São Paulo (FAPESP, grants 2018/01258-5, 2020/08575-6, 2020/12986-1, 2022/11173-2, 2023/02232-8, and 2023/02561-1), the Conselho Nacional de Desenvolvimento Científico e Tecnológico (CNPq, grants 309412/2018-8, 140849/2020-3, 311226/2022-1, and 405800/2022-3), and the Coordenação de Aperfeiçoamento de Pessoal de Nível Superior (CAPES, finance code 001). Additional financial support was provided by the Royal Society Newton Mobility Grants (R1/191179). The authors thank the Brazilian Nanotechnology National Laboratory (LNNano), an open-access facility operated by the Brazilian Center for Research in Energy and Materials (CNPEM) under the Ministry of Science, Technology, and Innovation (MCTI), for access to TEM analyses (proposals 20233617 and 20233680). We acknowledge DESY (Hamburg, Germany), a member of the Helmholtz Association (HGF), for the provision of experimental facilities. Part of this research was performed at beamline P02.1 of PETRA III (proposal I-20230990 EC). The authors also thank Prof. Diego Muraca and Mr Guilherme K. Soares (University of Campinas) for performing preliminary TEM analyses, Prof. Kirsten M. Ø. Jensen (University of Copenhagen) for PDF analysis insights, and Prof. Andrew M. Beale (University College London/Research Complex at Harwell) for granting access to *operando* DRIFTS measurements at his facilities. Finally, the authors acknowledge the use of the language model ChatGPT (OpenAI) for assistance in improving the English grammar and readability of the text. All scientific content, interpretations, and conclusions are solely the responsibility of the authors.

References

1 J. Ethiraj, D. Wagh and H. Manyar, *Energy Fuels*, 2022, **36**, 1189–1204.
2 L. Qu, X. Jiang, Z. Zhang, X. Zhang, G. Song, H. Wang, Y. Yuan and Y. Chang, *Green Chem.*, 2021, **23**, 9348–9376.
3 C. M. Michailof, K. G. Kalogiannis, T. Sfetsas, D. T. Patiaka and A. A. Lappas, *WIREs Energy Environ.*, 2016, **5**, 614–639.
4 R. J. M. Westerhof, D. W. F. Brilman, M. Garcia-Perez, Z. Wang, S. R. G. Oudenhoven, W. P. M. van Swaaij and S. R. A. Kersten, *Energy Fuels*, 2011, **25**, 1817–1829.

Open Access Article. Published on 27 April 2026. Downloaded on 5/21/2026 11:31:09 AM. This article is licensed under a Creative Commons Attribution-NonCommercial 3.0 Unported Licence.

5 I. Barroso-Martín, D. Ballesteros-Plata, A. Infantes-Molina, M. O. Guerrero-Pérez, J. Santamaría-González and E. Rodríguez-Castellón, *IET Renew. Power Gen.*, 2022, **16**, 3009–3022.
6 P. Sun, Z. Wang, C. Li, B. Tang and C. Peng, *Fuel*, 2024, **361**, 130726.
7 S. Haida, S. Löbner, H. Lund, S. Bartling, C. Kreyenschulte, H. Atia, A. M. Abdel-Mageed, C. Kubis and A. Brückner, *Catal. Sci. Technol.*, 2024, **14**, 2201–2217.
8 H. Zhang, J. Zhang, Y. Ma, Z. Cai, Y. Cao, K. Huang and L. Jiang, *Appl. Catal., A*, 2025, **699**, 120278.
9 G. B. Báfero, G. B. Strapasson, D. S. Leite and D. Zanchet, *ChemCatChem*, 2023, **15**, e202300663.
10 K. A. Goulas, A. V. Mironenko, G. R. Jenness, T. Mazal and D. G. Vlachos, *Nat. Catal.*, 2019, **2**, 269–276.
11 M. Shetty, D. Zanchet, W. H. Green and Y. Román-Leshkov, *ChemSusChem*, 2019, **12**, 2171–2175.
12 M. Shetty, K. Murugappan, T. Prasomsri, W. H. Green and Y. Román-Leshkov, *J. Catal.*, 2015, **331**, 86–97.
13 M. Shetty, K. Murugappan, W. H. Green and Y. Román-Leshkov, *ACS Sustain. Chem. Eng.*, 2017, **5**, 5293–5301.
14 X. Zhang, J. Tang, Q. Zhang, Q. Liu, Y. Li, L. Chen, C. Wang and L. Ma, *Catal. Today*, 2019, **319**, 41–47.
15 A. Saraeian, S. J. Burkhow, D. Jing, E. A. Smith and B. H. Shanks, *ACS Sustain. Chem. Eng.*, 2021, **9**, 6685–6696.
16 W. Lv, X. Hu, Y. Zhu, Y. Xu, S. Liu, P. Chen, C. Wang and L. Ma, *Renew. Energy*, 2022, **188**, 195–210.
17 A. J. Kohler, C. H. Walter and B. H. Shanks, *ACS Catal.*, 2023, **13**, 14813–14827.
18 A. J. Kohler, M. H. Khan and B. H. Shanks, *ACS Catal.*, 2025, **15**, 4317–4330.
19 A. Kurlov, X. Huang, E. B. Deeva, P. M. Abdala, A. Fedorov and C. R. Müller, *Nanoscale*, 2020, **12**, 13086–13094.
20 J. Fan, X. Wu, A. Piñeiro-García, N. Boulanger, Y. Panecatl-Bernal, A. Ashok, S. Koroidov and E. Gracia-Espino, *ACS Appl. Nano Mater.*, 2021, **4**, 12270–12277.
21 H. Wang, S. Liu, H. Wang, J. Chao, T. Li, N. Ellis, W. Duo, X. Bi and K. J. Smith, *Catal. Rev.*, 2025, **67**, 57–129.
22 C. Ehinger, S. Pollitt, J. De Jesus Silva, X. Zhou, K. Sakamoto, M. Nachtegaal, O. Safonova and C. Copéret, *Chem. Sci.*, 2025, **16**, 5887–5896.
23 W. Jia, Q. Lu, T. Tian, G. Pan, R. Tan, B. He and J. Liu, *Nanoscale*, 2024, **16**, 18076–18085.
24 D.-X. Liu, X. Deng, Y.-F. Zhu, Z. Meng, X.-F. Sun, M.-M. Shi, H.-X. Zhong and J.-M. Yan, *Nano Res.*, 2024, **17**, 5801–5806.
25 C. Yu, S. Yu and L. Li, *Fuel*, 2022, **308**, 122038.
26 S. Kasiraju and L. C. Grabow, *AIChE J.*, 2018, **64**, 3121–3133.
27 Y. W. Cheah, M. A. Salam, P. Arora, O. Öhrman, D. Creaser and L. Olsson, *Sustain. Energy Fuels*, 2021, **5**, 2097–2113.
28 C. Peng, L. Gao, S. Yang and J. Sun, *Chem. Commun.*, 2008, 5601.
29 W. Xu, P. J. Ramírez, D. Stacchiola, J. L. Brito and J. A. Rodriguez, *Catal. Lett.*, 2015, **145**, 1365–1373.
30 M. A. Golubeva and A. L. Maximov, *Renewable Sustainable Energy Rev.*, 2025, **210**, 115153.
31 S. Haida, S. Löbner, H. Lund, S. Bartling, C. Kreyenschulte, H. Atia, A. M. Abdel-Mageed, C. Kubis and A. Brückner, *Catal. Sci. Technol.*, 2024, **14**, 2201–2217.
32 I. E. Wachs and K. Routray, *ACS Catal.*, 2012, **2**, 1235–1246.
33 S. Chapman, C. Brookes, M. Bowker, E. K. Gibson and P. P. Wells, *Faraday Discuss.*, 2016, **188**, 115–129.
34 S. Posada-Pérez, P. J. Ramírez, R. A. Gutiérrez, D. J. Stacchiola, F. Viñes, P. Liu, F. Illas and J. A. Rodriguez, *Catal. Sci. Technol.*, 2016, **6**, 6766–6777.
35 M. Shetty, B. Buesser, Y. Román-Leshkov and W. H. Green, *J. Phys. Chem. C*, 2017, **121**, 17848–17855.
36 D. S. Leite, G. B. Strapasson and D. Zanchet, *Mol. Catal.*, 2022, **530**, 112623.
37 G. B. Strapasson, L. S. Sousa, G. B. Báfero, D. S. Leite, B. D. Moreno, C. B. Rodella and D. Zanchet, *Appl. Catal., B*, 2023, **335**, 122863.
38 G. B. Strapasson, G. B. Báfero, D. S. Leite, D. B. L. Santos, Â. Albuquerque, I. D. Barcelos, L. M. Rossi, C. B. Rodella and D. Zanchet, *Appl. Catal., B*, 2025, **373**, 125316.
39 P. Nunes, G. Strapasson, G. Báfero and D. Zanchet, *J. Braz. Chem. Soc.*, 2024, **35**, e20240126.
40 T. Suzuki, T. Yabe and K. Yamaguchi, *J. Jpn. Pet. Inst.*, 2025, **68**, 150–161.
41 M. M. Sullivan and A. Bhan, *ACS Catal.*, 2016, **6**, 1145–1152.
42 M. Ma, Y. Li, J. Lu, J. Li, M. Zhang, H. Yan, Y. Liu, X. Chen, Z. Meng and C. Yang, *Fuel*, 2026, **406**, 137160.
43 A. W. Sleight and B. L. Chamberland, *Inorg. Chem.*, 1968, **7**, 1672–1675.
44 D. S. Sawant, S. B. Kulkarni, D. P. Dubal and G. M. Lohar, Battery, *Energy*, 2025, **4**, e20240073.
45 https://icsd.fiz-karlsruhe.de/index.xhtml.
46 Y. Zhang, Y. Teng, Y. Li, X. Du, L. Liu, Y. Wu, Y. Meng, Y. Hua, X. Zhao and X. Liu, *Ionics*, 2019, **25**, 4361–4370.
47 Z. Zhao, X. Qi, Y. He, N. Li, H. Lai, B. Liu, Y. Chen and T. Jin, *Microchim. Acta*, 2024, **191**, 159.
48 S. Hajebi and A. Abedini, *J. Mater. Sci.: Mater. Electron.*, 2016, **27**, 4489–4493.
49 Y. Zhang, G. Zhao, Y. Jiang, W. Hong, Y. Zhang, M. Deng, H. Shuai, W. Xu, G. Zou, H. Hou and X. Ji, *ChemElectroChem*, 2019, **6**, 1688–1695.
50 N. F. Dummer, Z. Sodiq-Ajala, D. J. Morgan and T. E. Davies, *Catal. Commun.*, 2022, **163**, 106414.
51 Z. Lin, R. Chen, Z. Qu and J. G. Chen, *Green Chem.*, 2018, **20**, 2679–2696.
52 J. A. Rodriguez, J. Y. Kim, J. C. Hanson and J. L. Brito, *Catal. Lett.*, 2002, **82**, 103–109.
53 T. Prasomsri, M. Shetty, K. Murugappan and Y. Román-Leshkov, *Energy Environ. Sci.*, 2014, **7**, 2660–2669.
54 K. Murugappan, E. M. Anderson, D. Teschner, T. E. Jones, K. Skorupska and Y. Román-Leshkov, *Nat. Catal.*, 2018, **1**, 960–967.
55 G. Nazri, *Solid State Ion.*, 1992, **53–56**, 376–382.
56 H. Knoezinger and H. Jeziorowski, *J. Phys. Chem.*, 1978, **82**, 2002–2005.
57 L. Seguin, M. Figlarz, R. Cavagnat and J.-C. Lassègues, *Spectrochim. Acta, Part A*, 1995, **51**, 1323–1344.
58 J. F. Flores-Aguilar, I. S. Ibarra, A. Guevara-Lara and I. Vázquez-Garrido, *Appl. Spectrosc. Rev.*, 2024, **59**, 601–631.

© 2026 The Author(s). Published by the Royal Society of Chemistry

Open Access Article. Published on 27 April 2026. Downloaded on 5/21/2026 11:31:09 AM.
This article is licensed under a Creative Commons Attribution-NonCommercial 3.0 Unported Licence.

59 B. Saravanakumar, G. Ravi, R. Yuvakkumar, V. Ganesh and R. K. Guduru, *Mater. Sci. Semicond. Process.*, 2019, **93**, 164–172.
60 N. U. H. L. Ali, S. Manoharan, P. Pazhamalai and S.-J. Kim, *J. Energy Storage*, 2022, **52**, 104784.
61 C. Bouchy, C. Pham-huu and M. J. Ledoux, *J. Mol. Catal. A Chem.*, 2000, **162**, 317–334.
62 T. Prasomsri, T. Nimmanwudipong and Y. Román-Leshkov, *Energy Environ. Sci.*, 2013, **6**, 1732.
63 I. A. de Castro, R. S. Datta, J. Z. Ou, A. Castellanos-Gomez, S. Sriram, T. Daeneke and K. Kalantar-zadeh, *Adv Mater*, 2017, **29**, 1701619.
64 P. Delporte, F. Meunier, C. Pham-Huu, P. Vennegues, M. J. Ledoux and J. Guille, *Catal. Today*, 1995, **23**, 251–267.
65 M. M. Sullivan, J. T. Held and A. Bhan, *J. Catal.*, 2015, **326**, 82–91.
66 M. W. Nolte, A. Saraeian and B. H. Shanks, *Green Chem.*, 2017, **19**, 3654–3664.
67 M. W. Nolte, J. Zhang and B. H. Shanks, *Green Chem.*, 2016, **18**, 134–138.
68 D. G. B. Dionizio, L. Forrer, G. Berhault, P. M. de Souza and C. A. Henriques, *Mol. Catal.*, 2023, **536**, 112882.
69 H. Yang, X. Zhu, H. W. Amini, B. Fachri, M. Ahmadi, G. H. ten Brink, P. J. Deuss and H. J. Heeres, *Appl. Catal., A*, 2023, **654**, 119062.
70 C. R. Almeida de Abreu, L. R. Francisco, R. C. Rabelo-Neto, R. P. Floro Bonfim, M. E. Huguenin Maia da Costa, F. B. Noronha, P. M. de Souza and F. S. Toniolo, *Catal. Today*, 2025, **446**, 115120.
71 Q. Guo, M. Wu, K. Wang, L. Zhang and X. Xu, *Ind. Eng. Chem. Res.*, 2015, **54**, 890–899.
72 M. Zhang, J. Du and Y. Chen, *Catal. Sci. Technol.*, 2023, **13**, 1345–1357.
73 C. Wang, C. Wu, L. Deng, R. Zhang, S. Zhou, Z. Wang, C. Qiao and Y. Tian, *Fuel*, 2023, **353**, 129233.
74 P. Koley, S. Chandra Shit, B. Joseph, S. Pollastri, Y. M. Sabri, E. L. H. Mayes, L. Nakka, J. Tardio and J. Mondal, *ACS Appl. Mater. Interfaces*, 2020, **12**, 21682–21700.
75 F. Dong, Y. Zhu, H. Zheng, Y. Zhu, X. Li and Y. Li, *J. Mol. Catal. A: Chem.*, 2015, **398**, 140–148.
76 D. Konadu, C. R. Kwawu, R. Tia, E. Adei and N. H. de Leeuw, *Catalysts*, 2021, **11**, 523.
77 S. Gupta, A. Rajan, E. Fako, T. J. Goncalves, I. B. Müller, J. J. Varghese, A. Schäfer and S. De, *J. Phys. Chem. C*, 2025, **129**, 6262–6274.